Title

ESCRT-II/Vps25 Constrains Digit Number by Endosome-Mediated Selective Modulation of FGF-SHH Signaling

Journal

Cell Reports, 9(2)

ISSN

2639-1856

Authors

Handschuh, Karen
Feenstra, Jennifer
Koss, Matthew
et al.

Publication Date

2014-10-01

DOI

10.1016/j.celrep.2014.09.019

Peer reviewed

Article

Cell Reports

ESCRT-II/Vps25 Constrains Digit Number by Endosome-Mediated Selective Modulation of FGF-SHH Signaling

Graphical Abstract

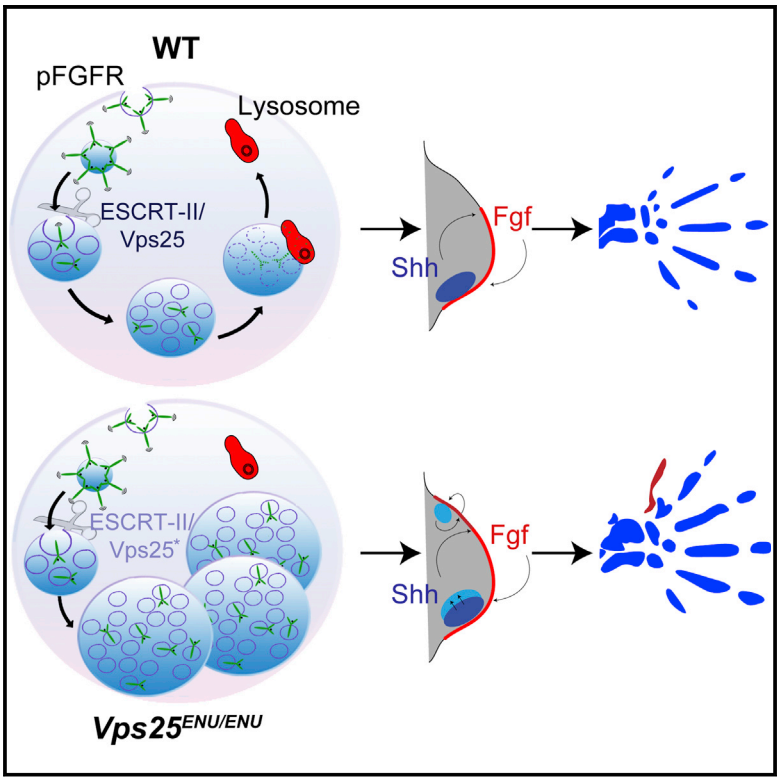

Highlights

ENU-induced mutation of mouse ESCRT-II/Vps25 causes polydactyly

Vps25 hypomorphic mutants survive until late gestation unlike ESCRT LOF embryos

ESCRT-II constrains digit number by endosome-mediated modulation of FGF signaling

Mutations in ESCRT reveal a mechanism underlying congenital limb defects

Authors

Karen Handschuh, Jennifer Feenstra, ..., Elizabeth Lacy, Licia Selleri

Correspondence

lis2008@med.cornell.edu

In Brief

Using a polydactylous mouse line carrying a hypomorphic mutation in the Vps25 subunit of the ESCRT-II complex, Handschuh et al. now establish that ubiquitously expressed machineries that sort signaling proteins preferentially regulate, or are rate limiting for, select signaling pathways in different contexts of the developing embryo.

Handschuh et al., 2014, Cell Reports 9, 674–687
October 23, 2014 ©2014 The Authors
http://dx.doi.org/10.1016/j.celrep.2014.09.019

OPEN ACCESS
CellPress

Cell Reports
Article

ESCRT-II/Vps25 Constrains Digit Number by Endosome-Mediated Selective Modulation of FGF-SHH Signaling

Karen Handschuh,[1,12] Jennifer Feenstra,[1,12] Matthew Koss,[1,12] Elisabetta Ferretti,[1] Maurizio Risolino,[1] Rediet Zewdu,[1] Michelle A. Sahai,[2] Jean-Denis Bénazet,[1] Xiao P. Peng,[1] Michael J. Depew,[3,4] Laura Quintana,[1,5] James Sharpe,[5,6,7] Baolin Wang,[8] Heather Alcorn,[9] Roberta Rivi,[9] Stephen Butcher,[10] J. Robert Manak,[10] Thomas Vaccari,[11] Harel Weinstein,[2] Kathryn V. Anderson,[9] Elizabeth Lacy,[9] and Licia Selleri[1,*]

[1]Department of Cell and Developmental Biology, Weill Cornell Medical College, New York, NY 10065, USA
[2]Department of Physiology and Biophysics, Weill Cornell Medical College, New York, NY 10065, USA
[3]Department of Craniofacial Development, King's College London, Guy's Hospital, London Bridge, London SE1 9RT, UK
[4]Department of Othopaedic Surgery, UCSF, San Francisco, CA 94110, USA
[5]Centre for Genomic Regulation (CRG), 08003 Barcelona, Spain
[6]Universitat Pompeu Fabra (UPF), 08003 Barcelona, Spain
[7]Institucio Catalana de Recerca i Estudis Avancats (ICREA), 08010 Barcelona, Spain
[8]Department of Genetic Medicine, Weill Cornell Medical College, New York, NY 10065, USA
[9]Developmental Biology Program, Sloan-Kettering Institute, New York, NY 10065, USA
[10]Departments of Biology and Pediatrics, University of Iowa, Iowa City, IA 52242, USA
[11]IFOM-FIRC Institute of Molecular Oncology, 20139 Milan, Italy
[12]Co-first author
*Correspondence: lis2008@med.cornell.edu
http://dx.doi.org/10.1016/j.celrep.2014.09.019

SUMMARY

Sorting and degradation of receptors and associated signaling molecules maintain homeostasis of conserved signaling pathways during cell specification and tissue development. Yet, whether machineries that sort signaling proteins act preferentially on different receptors and ligands in different contexts remains mysterious. Here, we show that Vacuolar protein sorting 25, Vps25, a component of ESCRT-II (Endosomal Sorting Complex Required for Transport II), directs preferential endosome-mediated modulation of FGF signaling in limbs. By ENU-induced mutagenesis, we isolated a polydactylous mouse line carrying a hypomorphic mutation of *Vps25* (*Vps25*^{ENU}). Unlike *Vps25*-null embryos we generated, *Vps25*$^{ENU/ENU}$ mutants survive until late gestation. Their limbs display FGF signaling enhancement and consequent hyperactivation of the FGF-SHH feedback loop causing polydactyly, whereas WNT and BMP signaling remain unperturbed. Notably, *Vps25*$^{ENU/ENU}$ Mouse Embryonic Fibroblasts exhibit aberrant FGFR trafficking and degradation; however, SHH signaling is unperturbed. These studies establish that the ESCRT-II machinery selectively limits FGF signaling in vertebrate skeletal patterning.

INTRODUCTION

The complexity of development is dependent upon signal transduction pathways, which are critical for cell specification, tissue patterning, organ morphogenesis, and growth. Notably, the embryo constructs markedly different structures by using the same signaling pathways (Wolpert, 1994). The developing vertebrate limb can serve as a tractable model to analyze mechanisms of cell signaling (Zeller, 2010).

In vertebrates, limb development is controlled by two signaling centers, the apical ectodermal ridge (AER) at the distal bud and the zone of polarizing activity (ZPA) in the posterior mesenchyme (Zeller, 2010). Both centers produce instructive signals that direct anterior-posterior (AP) and proximal-distal (PD) limb axis formation. The AER produces multiple fibroblast growth factors (FGF8, FGF4, FGF9, FGF17), whereas the ZPA produces Sonic Hedgehog (SHH) (Tabin and Wolpert, 2007). Throughout limb development, the AER and ZPA are interlinked by a feedback signaling loop, which is also influenced by other signaling molecules and transcription factors (Tabin and Wolpert, 2007; Zakany and Duboule, 2007; Zeller et al., 2009). Genetic mutations that perturb the FGF-SHH loop lead to alterations of the highly conserved pentadactyl pattern (Biesecker, 2011). Therefore, how cells maintain signaling homeostasis is critical for the establishment of digit number and identity.

Homeostasis of signaling proteins is maintained through sorting and degradation via endosome-mediated vesicular trafficking (MacGurn et al., 2012). Mutations of ESCRT (Endosomal Sorting Complex Required for Transport) machinery components compromise their ability to degrade conserved signaling proteins in

multiple organisms (Henne et al., 2011, 2013). Indeed, ESCRT LOF models display perturbations of signaling (Rusten et al., 2012). However, early lethality of mutants with complete LOF of ESCRT components (Rusten et al., 2012) and the absence of conditional or hypomorphic mutations has prevented understanding how ESCRT members contribute to shaping organismal forms. Furthermore, whether constitutively expressed multicomponent ESCRT machineries act on different receptors and associated signaling proteins in a specialized or preferential manner in different contexts of the developing embryo remains poorly understood.

Here, identification of a hypomorphic mutation in the ESCRT-II complex in a polydactylous mouse line isolated by a N-ethyl-N-nitrosourea (ENU) mutagenesis screen (Anderson and Ingham, 2003; Stottmann and Beier, 2010) allowed deconstruction of the mechanisms by which specific ESCRT components execute patterning and morphogenetic processes. This unique mouse model with a partially functional ESCRT-II allele afforded testing of the hypothesis that ubiquitously expressed ESCRT machineries act on different receptors and associated signaling proteins in a preferential manner in different embryonic contexts, such as the developing limb bud.

RESULTS

Isolation of *04-014* Mouse Line with Polydactyly through an N-ethyl-N-nitrosourea Mutagenesis Screen and Identification of the ENU-Induced Mutation in the *Vps25* Gene

By a N-ethyl-N-nitrosourea (ENU) mutagenesis screen, we isolated mouse line *04-014* based on recessive hindlimb polydactyly with variable expressivity (Figure 1A–1D). We located the mutation within the murine ortholog of yeast Vacuolar protein sorting 25, *Vps25* (also known as *EAP20*), encoding a subunit of the ESCRT-II complex (Babst et al., 2002b; Slater and Bishop, 2006) essential for endosomal protein trafficking (Henne et al., 2011; MacGurn et al., 2012; Rusten et al., 2012) (Figures 1E; Table S1). Identified by sequencing of candidate gene cDNA, and confirmed by deep sequencing (Arnold et al., 2011) of the narrowest genomic interval linked to the mutation (Table S1), a G-to-A transition in *Vps25* third intron generated an mRNA splice variant containing an in-frame 27-nucleotide insertion encoding nine additional neutral amino acids (Figures 1E–1G and S1A; Table S2). Hereafter, the ENU-induced allele will be designated $Vps25^{ENU}$ and the recessive homozygous mutant embryos $Vps25^{ENU/ENU}$.

ENU-Induced Mutation of ESCRT-II/*Vps25* Results in a Partially Functional Hypomorphic Allele, whereas LOF Causes Early Gestational Lethality

To characterize effects of the ENU-induced mutation on *Vps25* transcription, quantitative RT-PCR (qRT-PCR) detected the *Vps25* splice variant as well as wild-type (WT) mRNA in the mutants. However, in mutant embryos at various gestational days, both mRNA species and their encoded proteins were significantly less abundant than WT *Vps25* in WT littermates (Figures 1H, 1I, and S1B). Thus, the ENU-induced allele is hypomorphic, affording analysis of how ESCRT-II/Vps25 execute patterning and morphogenesis in vertebrate development.

To elucidate the requirements for *Vps25* during development, we compared the activity of $Vps25^{ENU}$ to a *Vps25* global LOF allele ($Vps25^{LacZ}$) we generated by replacing *Vps25* with a LacZ/Neo cassette (www.komp.org). At E8.5 no $Vps25^{LacZ/LacZ}$ embryos were recovered, only empty deciduae, defining the *Vps25* LOF allele as more deleterious than $Vps25^{ENU}$ (Figure S1C). Thus, similar to LOF of other mouse ESCRT components (Komada and Soriano, 1999; Lee et al., 2007; Ruland et al., 2001; Shim et al., 2006; Yamada et al., 2002), global *Vps25* LOF causes early lethality in utero. Consistent with early lethality, RT-PCR and X-gal staining of $Vps25^{LacZ/+}$ embryos corroborated widespread *Vps25* expression, including in limbs, from E9.5-E13.5 (Figures 1J–1M and S1D–S1J). Absence of complementation between $Vps25^{LacZ}$ and $Vps25^{ENU}$ in transheterozygous $Vps25^{LacZ/ENU}$ embryos confirmed the G-to-A transition in *Vps25* intron 3 as the causative mutation (Figures 1N–1Q; Table S3). As predicted for a hypomorphic allele, $Vps25^{ENU/ENU}$ embryos survived until E15.5–16.5 on a mixed genetic background (Figure 1Q), whereas $Vps25^{LacZ/ENU}$ embryos exhibited developmental delay and hemorrhaging as early as E9.5 (Figure 1P).

ENU-Induced Mutation of ESCRT-II/*Vps25* Causes Fully Penetrant Polydactyly

Skeletal preparations and Optical Projection Tomography (Sharpe et al., 2002) (OPT) revealed fully penetrant hindlimb polydactyly (Figures 2A–2D; Movies S1 and S2), whereas in mutant forelimbs polydactyly was less severe and not fully penetrant (Figures S2A–S2F′; Movies S3 and S4). Compared to WT, the mutant scapular blade was thinner with a central hole (Figures S2G and S2G′). Mutant limbs also exhibited shorter and thicker skeletal elements (Figures 2A, 2B, and S2H–S2L′).

To uncover the cellular behaviors underlying the polydactyly, we examined proliferation (Koss et al., 2012) and apoptosis (Ferretti et al., 2011) in WT and $Vps25^{ENU/ENU}$ limbs (Figures 2E–2L). E12.5 WT hindlimb showed a highly proliferative mesenchyme and a quiescent anterior AER (Figures 2E and 2G). In contrast, hindlimb anterior AER of $Vps25^{ENU/ENU}$ littermates appeared strikingly proliferative (Figures 2F and 2H). Additionally, unlike WT (Figures 2I and 2K), $Vps25^{ENU/ENU}$ anterior hindlimb contained no detectable cell death (Figures 2J, 2L, and S2U–S2X). We observed similar, albeit less pronounced, proliferation and apoptosis defects in $Vps25^{ENU/ENU}$ forelimbs (Figures S2M–S2T). *Msx2*, a marker of apoptotic cells (Lallemand et al., 2009), was expressed in the interdigital spaces and around digit 1 of E13.5 WT hindlimb; however, $Vps25^{ENU/ENU}$ hindlimb bud lacked *Msx2* in the domain where polydactyly arises (Figures 2M and 2N). Last, *Sox9* expression (Mariani and Martin, 2003) appeared diffuse in E13.5 $Vps25^{ENU/ENU}$ hindlimb anterior mesenchyme, suggesting multiple digit condensations (Figures 2O and 2P). These results implicate perturbations of proliferation and cell death in $Vps25^{ENU/ENU}$ anterior limb domains as the underlying causes of polydactyly or synpolydactlyly.

$Vps25^{ENU/ENU}$ Early Limb Buds Exhibit Specific Enhancement of the FGF-SHH Cross-Regulatory Loop Underlying Polydactyly, whereas WNT and BMP Signaling Are Unperturbed

To assess whether *Vps25* mutation induced ESCRT-II-dependent perturbation of signaling molecules critical for limb

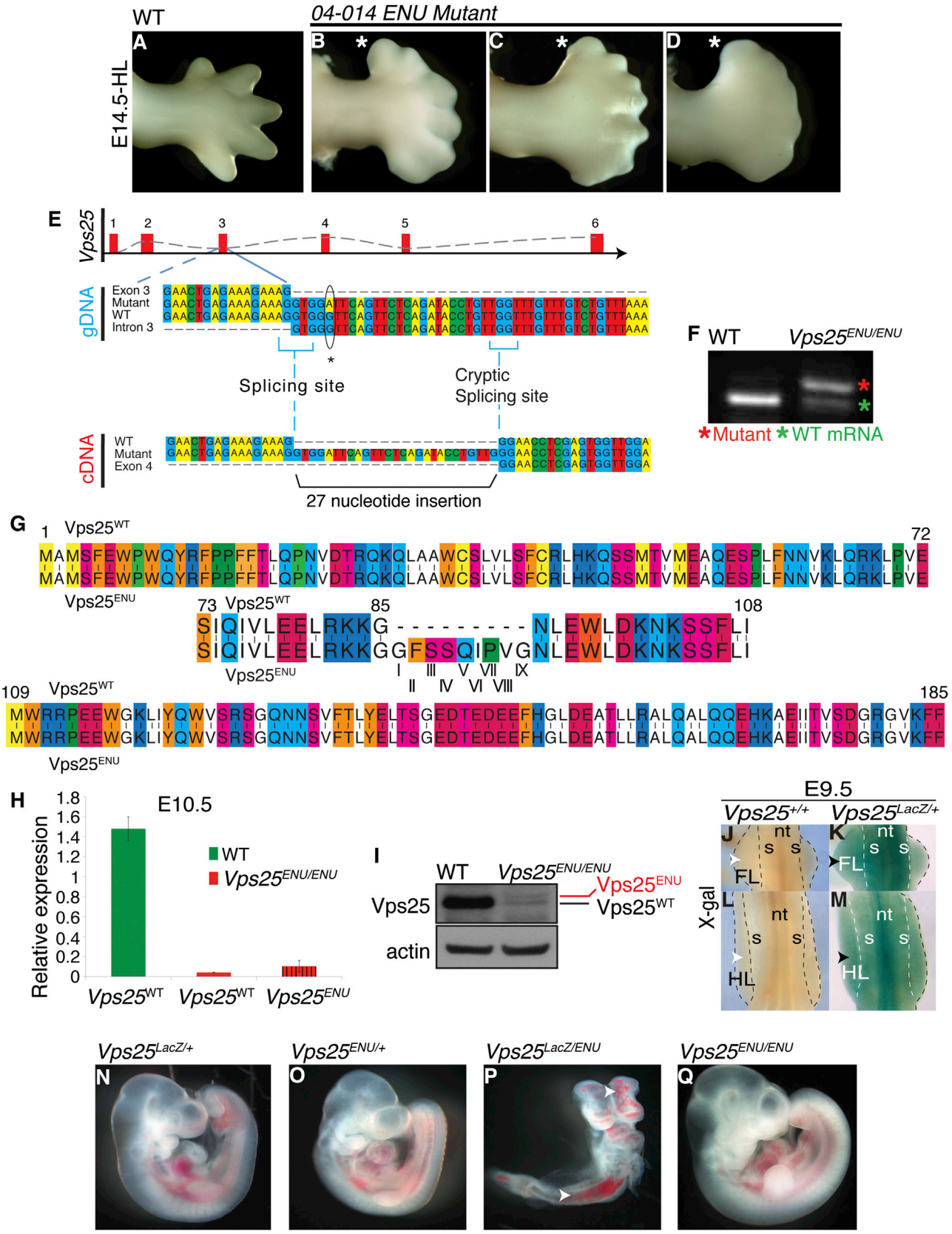

(legend on next page)

patterning, we analyzed their expression by whole-mount in situ hybridization (Figure 3). We examined the signaling loop between AER-FGF and ZPA-SHH. SHH activation requires not only FGFs, but also Hand2 and 5′ HoxD transcription factors (Zakany and Duboule, 2007). Notably, perturbations of 5′ *Hox* genes on *Gli3*-null background (Lopez-Rios et al., 2012) yield more severe polydactyly than LOF of *Gli3* alone (Sheth et al., 2012). In E10.5 $Vps25^{ENU/ENU}$ hindlimb, AER-*Fgf4* was expanded anteriorly (Figures 3A), whereas ZPA-*Shh* expression was not perturbed (Figure 3B). At E11–11.5, $Vps25^{ENU/ENU}$ hindlimb *Fgf4* and mesenchymal *Gremlin* (Verheyden and Sun, 2008) were expanded anteriorly (Figures 3C, 3D, and S3A) as was *Shh* expression, whereas *Fgf8* was unperturbed (Figure 3E). Consistent with ZPA-*Shh* expansion, *Patched1* was upregulated in E11.5 $Vps25^{ENU/ENU}$ hindlimb (Figure 3F). Moreover, significantly increased *Shh* and *Patched1* mRNA levels were detected by qRT-PCR in E11.5 $Vps25^{ENU/ENU}$ *versus* WT hindlimbs (Figure 3G and 3H). In addition, western blot on whole-limb lysates demonstrated greater reduction of Gli3 repressor (Gli3R) (Wang et al., 2000) levels in $Vps25^{ENU/ENU}$ hindlimb (Figures 3I and S3B) versus forelimb (Figure S3C). Furthermore, in E11.5 $Vps25^{ENU/ENU}$ anterior hindlimb, ectopic expression of *Hand2*, *HoxD13*, and *Gli1*, as well as downregulation of *Gli3*, were observed before *Shh* ectopic anterior expression could be detected at E12–12.5 (Figures 3J–3N). Of note, in E12.5 mutant hindlimb, *Shh* persisted in the ZPA (Figure 3N), *Fgf4* and *Fgf8* were still present in anterior AER (Figures 3O and 3P), and *Sprouty2* was therein upregulated (Figure 3Q). Also, ectopic *Gli1* and *HoxD13* were still manifest in E12.5 $Vps25^{ENU/ENU}$ hindlimb (Figures S3D and S3E). Intriguingly, whereas bone morphogenic protein (BMP) activity is required to regulate digit number (Selever et al., 2004), early BMP as well as WNT signaling components (Zeller, 2010) appeared unperturbed in E11 mutant hindlimbs (Figures S3F–S3K). These results establish selective enhancement of the FGF-SHH cross-signaling loop in $Vps25^{ENU/ENU}$ limb patterning.

The WT ESCRT-II/Vps25-ESCRT-III/Vps20 Complex Is Mostly Detected within Late Endosomes, whereas the Mutant $Vps25^{ENU}$-Vps20 Complex Is Diffuse throughout the Cytoplasm

To test whether the nine amino acid insertion into the $Vps25^{ENU}$ protein in mutant embryos led to perturbed function, we assessed cellular localization of transfected FLAG- or HA-tagged WT and $Vps25^{ENU}$ cDNA constructs expressed alone or in combination. Regardless of the tag, WT and $Vps25^{ENU}$ proteins colocalized within the cytoplasm, also within distinct puncta (Figures 4A–4G). Coimmunoprecipitation of WT and $Vps25^{ENU}$ proteins by tag-specific antibodies followed by western blotting with an anti-Vps25 antibody (Langelier et al., 2006) showed that Vps25 ENU-induced mutation does not inhibit heterodimerization of Vps25 mutant protein with WT (Figure 4H). Furthermore, cotransfected WT or $Vps25^{ENU}$ proteins colocalized within the cytoplasm and coimmunoprecipitated with Vps20, a component of the ESCRT-III complex that binds to ESCRT-II via its Vps25 subunit (Babst et al., 2002a; Im et al., 2009), suggesting that both WT and $Vps25^{ENU}$ proteins can recruit Vps20 (Figures 4I–4O). Given colocalization with the late endosome marker Lamp1 (Shim et al., 2006), but not EEA1, which stains early endosomes, cytoplasmic puncta containing either WT or mutant Vps25-Vps20 complex are late endosomes (Figure S4). However, whereas the WT Vps25-Vps20 protein complex was predominantly localized within late endosomes, the mutant $Vps25^{ENU}$-Vps20 complex appeared mostly diffuse throughout the cytoplasm (Figures 4I–4N). Because interactions between ESCRT-II and ESCRT-III are critical for scission of cargo-filled vesicles into the developing endosome (Im et al., 2009), mislocalization of the mutant complex likely contributes to disruption of vesicular trafficking.

Structural Rigidification of the $Vps25^{ENU}$ Protein Underlies Abnormal Subcellular Localization of the Mutant ESCRT-II/ESCRT-III Complex with Perturbed Lysosome-Mediated Trafficking and Impaired Degradation of Cargo

To determine whether the nine amino acid insertion (Figure 1G) affects the conformation and dynamics of the mutant protein, we used computational modeling of the $Vps25^{ENU}$ protein structure. In three separate simulations of Vps25 WT and mutant proteins, the WH2 domain (Im and Hurley, 2008) in $Vps25^{ENU}$ was found to be less flexible than in WT (Figures 5A and S5A–S5C). Analyses of conformational changes and fluctuations identified a stabilizing hydrogen bond in $Vps25^{ENU}$ between a residue from the ENU-induced insertion, Ser (IV), and Glu (105+9) (Figures 5A and S5D). The structural context observed from

Figure 1. Identification of Polydactylous Mouse Line *04-014* by ENU Mutagenesis and Cloning of the ESCRT-II/*Vps25* Hypomorphic Mutation

(A–D) Gross morphology shows different expressivity of the polydactyly in E14.5 $Vps25^{ENU/ENU}$ hindlimbs, including a widened autopod with six (B) or seven (C) digits, or synpolydactyly (D) (domain of additional digits; white asterisk).

(E and F) Sequencing of *Vps25* genomic (g) and complementary (c) DNA detects a mutation (asterisk) within intron 3, five nucleotides downstream to the exon-intron border, resulting in a 27 nucleotide insertion in the mutant *Vps25* mRNA, visualized by PCR (F).

(G) Alignment of $Vps25^{WT}$ (top) (Protein UniProt/NCBI number: Q9CQ80) and $Vps25^{ENU}$ mutant (bottom) proteins shows a nine amino acid insertion starting at amino acid 86. $Vps25^{WT}$ protein contains two winged helix domains WH1 (amino acids 1–84) and WH2 (amino acids 84–176) (Langelier et al., 2006). The additional nine amino acids, indicated by roman numbers, reside within the Vps25 WH2 domain.

(H and I) qRT-PCR and western blot (WB) from E10.5 whole embryos demonstrate presence of WT Vps25 mRNA and protein, respectively, in $Vps25^{ENU/ENU}$ mutants. qRT-PCR, mean of two samples run in triplicate ± SEM; *Tbp* used for normalization.

(J–M) X-gal staining reveals ubiquitous *Vps25* expression, including forelimb (FL) and hindlimb (HL) (black arrowheads), in E9.5 $Vps25^{LacZ/+}$ embryos, versus lack of staining (white arrowheads) in WT. s, somites; nt, neural tube.

(N–Q) Delayed and abnormal development of $Vps25^{LacZ/ENU}$ double heterozygote (arrowheads indicate hemorrhaging) as early as E9.5 versus WT morphology of $Vps25^{LacZ/+}$ and $Vps25^{ENU/+}$ single heterozygotes proves that the $Vps25^{ENU}$ mutation is not complemented by the *Vps25* LOF allele. As predicted for a hypomorphic allele, $Vps25^{ENU/ENU}$ embryos survive until later in gestation and appear normal at E10.5 (Q).

See also Figure S1 and Tables S1–S3.

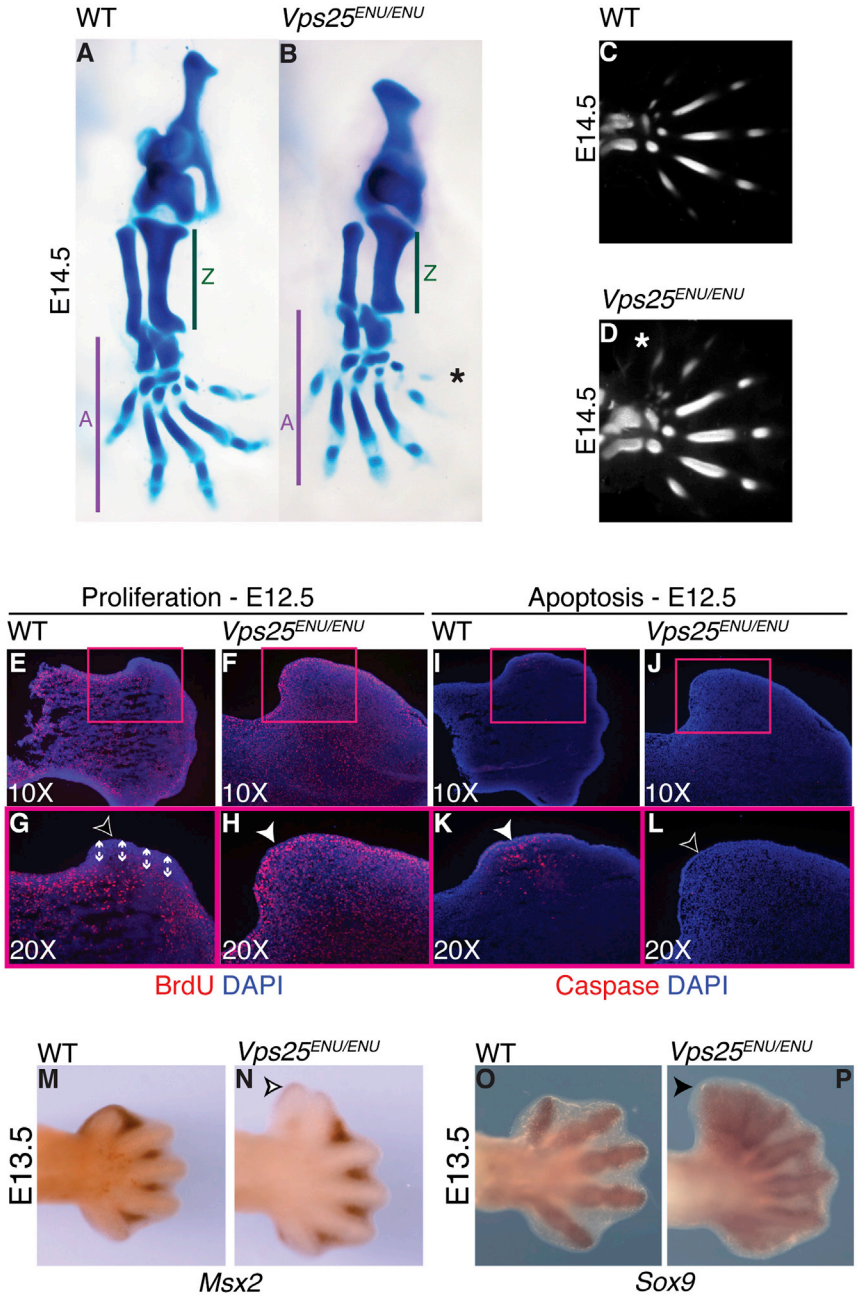

Figure 2. Preaxial Polydactyly, Proliferation, and Apoptosis Defects in *Vps25*$^{ENU/ENU}$ Mutant Hindlimb

(A and B) Shorter and thicker hindlimb (HL) zeugopod (Z) and preaxial polydactyly (asterisk) in E14.5 *Vps25*$^{ENU/ENU}$ autopod (A) by Alcian blue staining.

(C and D) OPT shows polydactyly (asterisk) in E14.5 *Vps25*$^{ENU/ENU}$ HL.

(E–L) BrdU and cleaved Caspase-3 IF reveals increased proliferation (white arrowhead) and decreased apoptosis (empty arrowhead) in E12.5 *Vps25*$^{ENU/ENU}$ anterior HL.

(M–P) In situ hybridization shows loss of *Msx2* (empty arrowhead) and increased *Sox9* (black arrowhead) mRNA in E13.5 *Vps25*$^{ENU/ENU}$ anterior HL.

See also Figure S2 and Movies S1 and S2.

the simulations attributes the greater conformational stability of the Vps25^{ENU} protein to the presence of stronger hydrogen bonds, one of which cannot form in the Vps25^{WT}. The increased rigidity of the Vps25^{ENU} framework might be unable to conform to the characteristic Y-shaped structure typical of ESCRT-II (Teis et al., 2010). Such a structural rigidification of the Vps25^{ENU} protein could potentially change its overall interaction with other ESCRT-II components like Vps22 and Vps36, as well as interactions with ESCRT-III (Im et al., 2009). Although Vps20/ESCRT-III is recruited to Vps25^{ENU}/ESCRT-II, the subcellular localization of the mutant Vps25^{ENU}-Vps20 complex is altered (Figures 4 and S4), suggesting perturbed degradation of signaling molecules.

To evaluate whether the *Vps25* ENU-induced mutation caused abnormal lysosome-mediated trafficking and degradation of cargo within the cell, we isolated mouse embryonic fibroblasts (MEFs) from WT and *Vps25*$^{ENU/ENU}$ embryos. Transmission electron microscopy (TEM) revealed significantly enlarged multivesicular bodies (MVBs, a form of late endosomes [Henne et al., 2011, 2013]) in mutant versus WT MEFs (Figures 5B–5D). Horseradish peroxidase (HRP) uptake experiments (Shim et al., 2006) followed by TEM showed that in *Vps25*$^{ENU/ENU}$ MEFs there are significantly higher numbers of HRP-positive MVBs than HRP-positive lysosomes (Figure 5E). Accordingly, in *Vps25*$^{ENU/ENU}$ MEFs HRP-positive lysosomes were negligible (Figure 5F). HRP pulse-chase experiments followed by western blotting with an anti-HRP antibody (Ab) confirmed HRP degradation defects in *Vps25*$^{ENU/ENU}$ MEFs (Figure 5G). Importantly, TEM revealed significantly enlarged MVBs also in vivo in limb bud AER as well as mesenchyme of E11.5 *Vps25*$^{ENU/ENU}$ embryos versus WT littermates (Figures 5H–5K). Altogether, these results indicate that in WT MEFs exogenous HRP is trafficked to lysosomes via MVBs, whereas in *Vps25*$^{ENU/ENU}$ MEFs HRP does not reach lysosomes for degradation and is trapped in engorged MVBs. The latter are significantly enlarged in cultured mutant MEFs and also in mutant limb bud compartments, demonstrating that similar abnormalities occur in vivo as a result of *Vps25* mutation.

In *Vps25*$^{ENU/ENU}$ Mouse Embryonic Fibroblasts, pFGFR Retained within Late Endosomes Leads to Increased Levels of FGF Second Messengers, whereas SHH Signaling Remains Unperturbed

To assess whether perturbed degradation generated enhancement of FGF and/or SHH signaling in a cellular system, as in

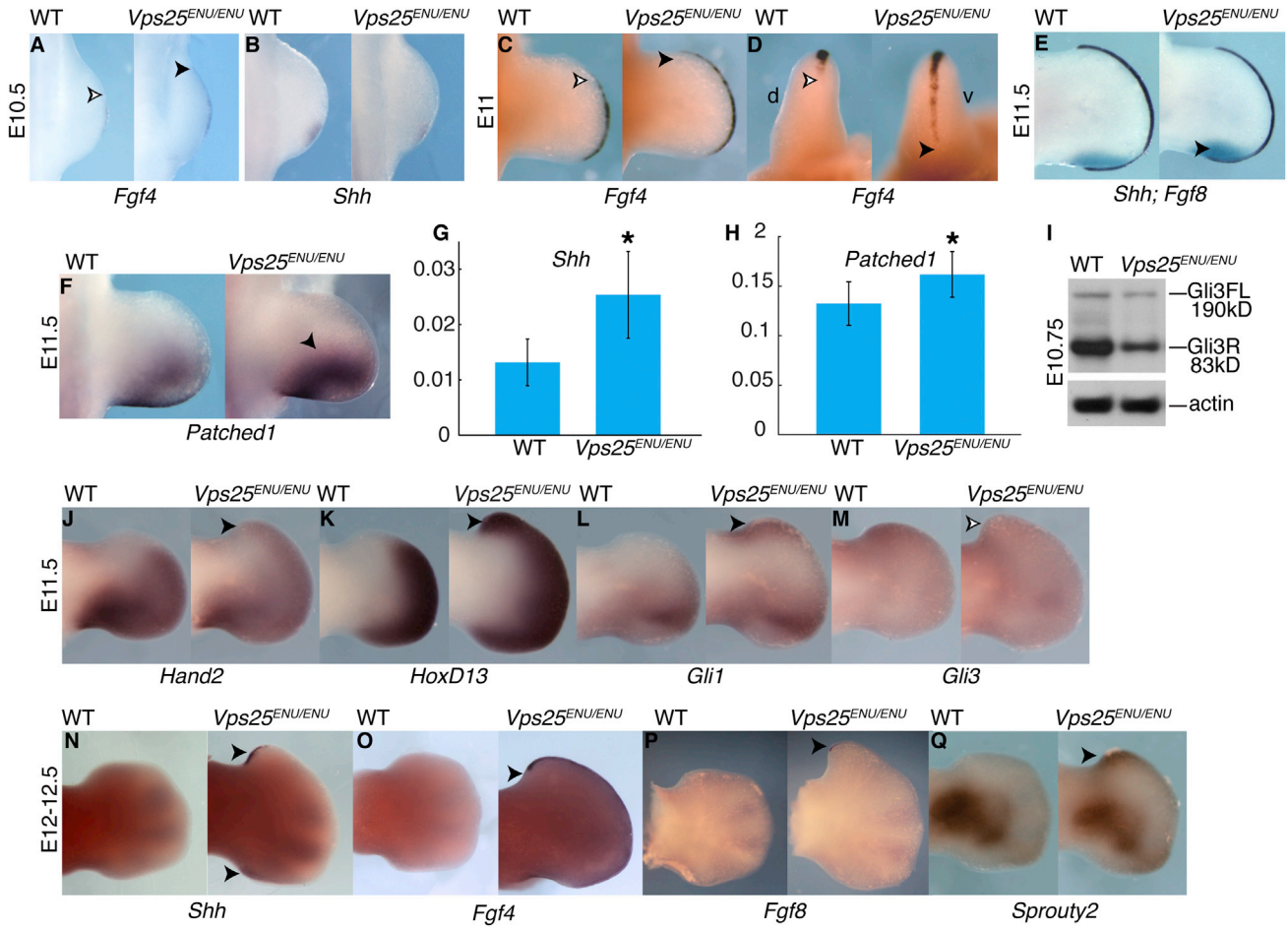

Figure 3. Selective Enhancement of the FGF-SHH Cross-Regulatory Loop in *Vps25*$^{ENU/ENU}$ Early HL Buds

(A–F) Expression of *Fgf4*, *Shh*, *Fgf8*, and *Patched1* by in situ hybridization of E10.5-E11.5 WT and *Vps25*$^{ENU/ENU}$ HL buds. (D) Anterior view.

(G and H) qRT-PCR of *Shh* and *Patched1* mRNAs from E11.5 WT and *Vps25*$^{ENU/ENU}$ HL buds; *Rpl19* as internal control. Bars represent the mean of three HL bud pairs run in triplicate ± SD (*$p < 0.05$).

(I) WB demonstrates altered Gli3 processing in E10.75 *Vps25*$^{ENU/ENU}$ HL, wherein levels of Gli3R are reduced. FL, full-length; R, repressor.

(J–Q) Expression of *Hand2*, *HoxD13*, *Gli1*, *Gli3*, *Shh*, *Fgf4*, *Fgf8*, and *Sprouty2* by in situ hybridization of E11.5-E12.5 WT and *Vps25*$^{ENU/ENU}$ HL buds.

Anterior, top; proximal, left; d, dorsal; v, ventral. Black arrowheads, spatially expanded, temporally protracted, and ectopic gene expression in mutant buds. Empty arrowheads, absence of signal. See also Figure S3.

Vps25$^{ENU/ENU}$ mutant limbs, we analyzed components of both pathways in WT and mutant MEFs. Pearson's coefficient analysis (Teis et al., 2008) of FGF4 pulse-chase experiments showed a 1.3-fold increase in colocalization of pFGFR and Lamp1 in *Vps25*$^{ENU/ENU}$ MEFs versus WT (Figures 6A–6G). Additionally, LysoTracker staining (Shim et al., 2006), which measures vesicular pH, was decreased by approximately 50% in *Vps25*$^{ENU/ENU}$ MEFs versus WT after FGF4 pulse-chase (Figures 6H–6J), supporting a defect in lysosomal functionality. Also, in WT MEFs, phospho-ERK (pERK) decreased within 1 hr of cycloheximide (CHX) treatment, whereas in *Vps25*$^{ENU/ENU}$ MEFs pERK levels, which were already higher than in WT before treatment, remained elevated for 2.5 hr, indicating abnormal endosome-mediated degradation (Figures 6K and 6L). Consistent with accumulation of pFGFR in *Vps25*$^{ENU/ENU}$ MEFs, we observed higher pERK and pSTAT3 (Hart et al., 2000) levels in E13.5 mutant whole embryos and E11.5 mutant versus WT limbs (Figure 6M). Kinetics of pSTAT3 activation versus degradation, in FGF pulse-chase experiments, revealed higher pSTAT3 levels in *Vps25*$^{ENU/ENU}$ MEFs versus WT (Figures 6N and 6O). In contrast, relative expression of SHH pathway components *Gli1* and *Patched1* was not significantly perturbed in *Vps25*$^{ENU/ENU}$ MEFs untreated or stimulated with the SHH agonist SAG (Goetz et al., 2009) versus WT (Figures 7A and 7B). Accordingly, Smoothened, a transducer of SHH signaling, did not accumulate in the engorged late endosomes of *Vps25*$^{ENU/ENU}$ MEFs (Figure 7C). Pearson's coefficient analysis of Smoothened trafficking in MEFs showed no colocalization of Smoothened and engorged Lamp1-positive endosomes in *Vps25*$^{ENU/ENU}$ MEFs untreated or stimulated with SAG (Figure 7D). Together, these results demonstrate that in *Vps25*$^{ENU/ENU}$ MEFs pFGFR is retained in late endosomes and does not reach lysosomes for degradation.

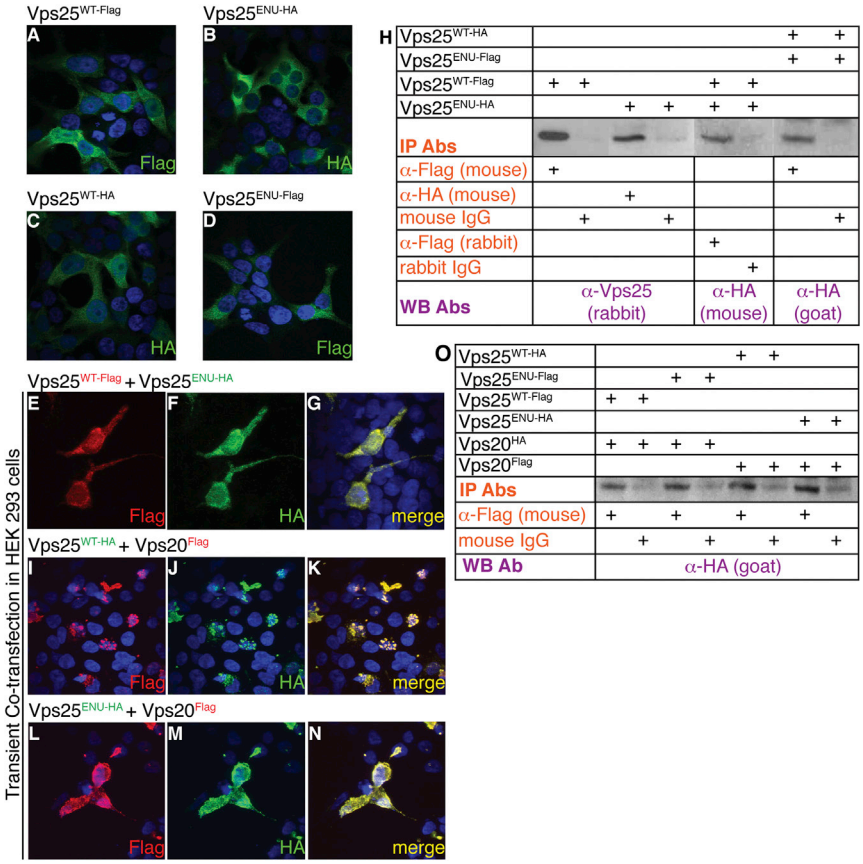

Figure 4. ESCRT-II/Vps25^{WT} and ESCRT-II/Vps25^{ENU} Immunoprecipitate with ESCRT-III/Vps20 Protein, and the WT Protein Complex Is Mostly Detected within Puncta, whereas the Mutant Complex Is Diffuse throughout the Cytoplasm

(A–G) Transient transfection of Vps25$^{WT\text{-}FLAG}$, Vps25$^{WT\text{-}HA}$, Vps25$^{ENU\text{-}HA}$, or Vps25$^{ENU\text{-}FLAG}$, alone or in combination, in HEK293 cells. IF with FLAG or HA antibodies (Ab) reveals that Vps25^{WT} and Vps25^{ENU} mutant proteins colocalize within the cytoplasm, also within puncta.

(H) Coimmunoprecipitation (IP) of Vps25 WT and mutant proteins from cells transfected with Vps25$^{WT\text{-}FLAG}$ and Vps25$^{ENU\text{-}HA}$ or with Vps25$^{WT\text{-}HA}$ and Vps25$^{ENU\text{-}FLAG}$. IP with anti-FLAG or anti-HA Ab; WB with anti-Vps25 or anti-HA.

(I–O) Both tagged Vps25^{WT} and Vps25^{ENU} colocalize and coimmunoprecipitate with tagged Vps20 in transfected HEK293 cells. However, subcellular localization of the mutant Vps25^{ENU}-Vps20 complex is diffuse throughout the cytoplasm, unlike the WT complex, which localizes to puncta.

Abs used for IP and WB labeled orange and purple, respectively. See also Figure S4.

Furthermore, FGF second messengers pERK and pSTAT3 are increased in *Vps25$^{ENU/ENU}$* embryos and MEFs, highlighting FGF signaling upregulation in both systems. Unexpectedly, SHH signaling is not intrinsically upregulated in *Vps25$^{ENU/ENU}$* MEFs and SHH pathway components do not accumulate within late endosomes, suggesting that SHH enhancement in mutant limbs results from selective hyperactive FGF signaling within the FGF-SHH feedback loop.

Inhibition of the FGF-SHH Signaling Loop via Reduction of SHH Dosage Rescues Polydactyly in *Vps25$^{ENU/ENU}$* Limbs

To determine whether polydactyly could be specifically ameliorated by limiting FGF-SHH cross-signaling in *Vps25$^{ENU/ENU}$* embryos, we reduced the dosage of SHH (Chiang et al., 2001). Genetic reduction of SHH in *Vps25$^{ENU/ENU}$;Shh$^{+/-}$* mutants partially rescued polydactyly (Figures 7E and S7A) by preventing *Fgf4* expansion present in *Vps25$^{ENU/ENU}$* anterior hindlimb AER (Figure 7E′; see also Figures 3A, 3C, and 3D). Seven digit hindlimbs decreased from 39% in *Vps25$^{ENU/ENU}$* mutant embryos to 14% in *Vps25$^{ENU/ENU}$;Shh$^{+/-}$* mutants, and pentadactyly, albeit with abnormally shaped digits, appeared in 27% of *Vps25$^{ENU/ENU}$;Shh$^{+/-}$* hindlimbs (Figure S7B). Partial genetic rescue of polydactyly in *Vps25$^{ENU/ENU}$;Shh$^{+/-}$* limbs demonstrates that ESCRT-II/Vps25 constrains digit number by specific modulation of the FGF-SHH cross-regulatory loop in the limb. Remarkably, loss of one allele of *Shh* did not partially rescue the craniofacial defects of *Vps25$^{ENU/ENU}$* embryos, consisting of hypoplastic jaw, stunted snout, and malformed ear pinna (Figure S7C). These findings strongly underscore that the Vps25 ENU-induced mutation preferentially and primarily affects FGF signaling in the limb bud and that SHH enhancement in *Vps25$^{ENU/ENU}$* mutant limbs results from hyperactivation of FGF signaling within the FGF-SHH feedback loop (Figures 7F and 7G).

DISCUSSION

ESCRT complex components, first identified in yeast, control multiple cellular functions, including receptor signaling, cytokinesis, autophagy, cell migration/motility, repair of plasma membrane wounds, miRNA activity, and mRNA localization/transport in metazoans (Henne et al., 2013; Jimenez et al., 2014; Rusten et al., 2012). Evidence supports requirements of ESCRT proteins in promoting endosome-mediated degradation of signaling receptors across the animal kingdom (MacGurn et al., 2012; Rusten et al., 2012). However, despite their reported roles in signal attenuation, in *Drosophila* Vps27/Hrs-Stam (ESCRT-0) promotes FGF signaling (Chanut-Delalande et al., 2010) and in *Xenopus* Vps4 acts as a positive regulator of WNT signaling (Taelman et al., 2010). This suggests a yet unexplored diversity in the regulation of signaling by ESCRT components (Tognon et al., 2014). Consistent with constitutive expression of ESCRT subunits and with their pleiotropic roles in trafficking of signaling proteins, LOF mutations of mouse ESCRT components result in early lethality in utero (E8–11) (Rusten et al., 2012). This has precluded dissection of specific ESCRT-dependent morphogenetic processes during

organ formation. Here, the ENU-induced hypomorphic mutation of murine ESCRT-II/Vps25 results in late embryonic lethality, thus affording deconstruction of unexplored ESCRT-II requirements in the control of signal transduction underlying mammalian tissue patterning. Using this unique model, we propose that ESCRT-II/Vps25 constrains digit number by exerting selective attenuation of FGF signaling and by consequently maintaining homeostasis of the FGF-SHH feedback loop in the developing limb. Interestingly, together with hyperactivation of FGF-SHH signaling in mutant $Vps25^{ENU/ENU}$ limbs, *Fgf* and *Shh* mRNAs are also upregulated suggesting a direct or indirect positive feedback whereby the increased protein levels cause upregulation of their own mRNAs. Alternatively, because ESCRT-II can directly affect mRNA localization acting as RNA binding proteins, ESCRT-II/Vps25 mutations might yield accumulation of select mRNAs within the cell (Irion and St Johnston, 2007). Last, mutations of Vps25/ESCRT-II might directly affect miRNA-mediated degradation of specific mRNAs (Gibbings et al., 2009), potentially including *Fgf* and *Shh*, in mutant limbs.

FGF signaling mediates multiple functions in embryonic development (Goetz and Mohammadi, 2013; Itoh and Ornitz, 2004). In limb bud mesenchyme, FGF4 stimulates proliferation (Niswander and Martin, 1993) and, together with FGF8, is required for cell survival (Sun et al., 2002). Although multiple reports link polydactyly to ectopic or enhanced SHH activity (Anderson et al., 2012), increased *Fgf4* expression in early mouse limbs causes polydactyly (Lu et al., 2006) and ectopic *Fgf4* expression in spontaneous mutant chickens initiates polydactyly independent of SHH activity (Bouldin and Harfe, 2009). Interestingly, $Vps25^{ENU/ENU}$ mutant hindlimbs exhibit *Fgf4* expansion before *Shh* perturbations arise, which alone could result in enhanced proliferation and lack of cell death causing polydactyly. FGF signaling has also critical roles in the control of endochondral bone development (Chen et al., 2014; Ornitz and Marie, 2002). Notably, limbs of $Vps25^{ENU/ENU}$ embryos display abnormally short and thick skeletal elements (Figures 2A, 2B, and S2F–S2L′), similar to humans with achondroplasia (dwarfism) (Ornitz and Marie, 2002). Achondroplastic patients and mouse models harboring activating mutations of the FGF pathway exhibit skeletal hypoplasia and epiphyseal growth plate dysmorphology (Naski et al., 1998). Due to edema and hemorrhaging in $Vps25^{ENU/ENU}$ embryos already at E14.0, it is impossible to determine whether their skeletal hypoplasia is due to cell-autonomous FGF activation in the growth plate until a mouse with *Vps25* conditional LOF is available. Nonetheless, the striking similarities of the skeletal phenotypes in these mouse mutants support a scenario whereby *Vps25* mutation disrupts bone development by perturbing FGF signaling, leading to achondroplastic phenotypes.

Intriguingly, in the developing limb not all signaling pathways are hyperactive, or otherwise altered, as a result of ESCRT-II complex impairment. For example, in $Vps25^{ENU/ENU}$ limbs at E11, when FGF signaling is hyperactive, early WNT and BMP signaling components appear unperturbed. This is worthy of note, because proper BMP activity is required to regulate digit number (Selever et al., 2004). In addition, in $Vps25^{ENU/ENU}$ mouse embryonic fibroblasts FGF signaling is upregulated, whereas SHH signaling is not intrinsically enhanced. Last, in $Vps25^{ENU/ENU}$ embryos, loss of one allele of *Shh* partially rescues polydactyly by preventing *Fgf4* expansion, whereas it does not partially rescue the craniofacial defects. Together, the findings in this model underscore preferential hyperactivation of FGF signaling as the main culprit of polydactyly in ESCRT-II/Vps25 mutant embryos. Alternatively, these results could suggest that during early limb patterning maintenance of homeostasis of most signaling pathways requires relatively low levels of ESCRT-II function, with a few exceptions such as the FGF pathway for which ESCRT function would become rate limiting in a context-specific manner. On the other hand, because Vps25 has been shown to control Notch and other signaling pathways in *Drosophila* (Thompson et al., 2005; Vaccari and Bilder, 2005), signaling cascades other than FGF might be affected in other domains of $Vps25^{ENU/ENU}$ embryos. In addition, within the limb bud proper, signaling mediated by other tyrosine kinase receptors might be concomitantly enhanced in $Vps25^{ENU/ENU}$ embryos and might contribute to polydactyly. In particular, expression of constitutively active EGFR in chick limbs in ovo causes polydactyly (Omi et al., 2005). Yet, in contrast to $Vps25^{ENU/ENU}$ embryos, developing limb buds with activated EGFR exhibit multiple, fragmented, or bifurcating ectopic AERs expressing *Fgf8*, as well as downregulation of *Bmp4*, resulting in pre- and postaxial polydactyly.

In summary, we isolated an ENU-induced hypomorphic mutation of ESCRT-II/Vps25 in a polydactylous mouse line, which allowed dissection of the mechanisms whereby ESCRT components execute mammalian limb patterning. The availability of this unique mouse model led us to establish that in the developing embryo ubiquitously expressed ESCRT machineries act on different receptors and associated signaling proteins in a preferential manner. In addition, our study demonstrates that ESCRT-mediated downregulation of specific signaling pathways appears more critical in certain embryonic contexts than in others. Although limb, craniofacial, and heart development are severely affected by the ESCRT-II/Vps25 mutation, development of other organ systems appears unperturbed. Our research demonstrates that ESCRT-II/Vps25 effects preferential modulation of FGF signaling in the mammalian limb, which, in turn, controls cellular proliferation and cell death establishing normal digit number and identity, as well as controlling skeletal maturation, relevant to congenital limb defects. Broadly, our study proposes a mechanism for signaling homeostasis in the vertebrate embryo highlighting that endosomal sorting by specific components of the ESCRT machinery preferentially regulates, or is rate limiting for, select conserved signaling pathways in distinct tissue patterning processes.

EXPERIMENTAL PROCEDURES

A detailed description of reagents and protocols is in the Supplemental Experimental Procedures. See the following experimental procedures for brief descriptions.

Generation of Mutant Line *04-014* by an N-ethyl-N-nitrosourea Mutagenesis Screen

Mutant mouse line *04-014* was generated by ENU mutagenesis of C57BL/6J males, as previously described (Anderson and Ingham, 2003; Stottmann and Beier, 2010).

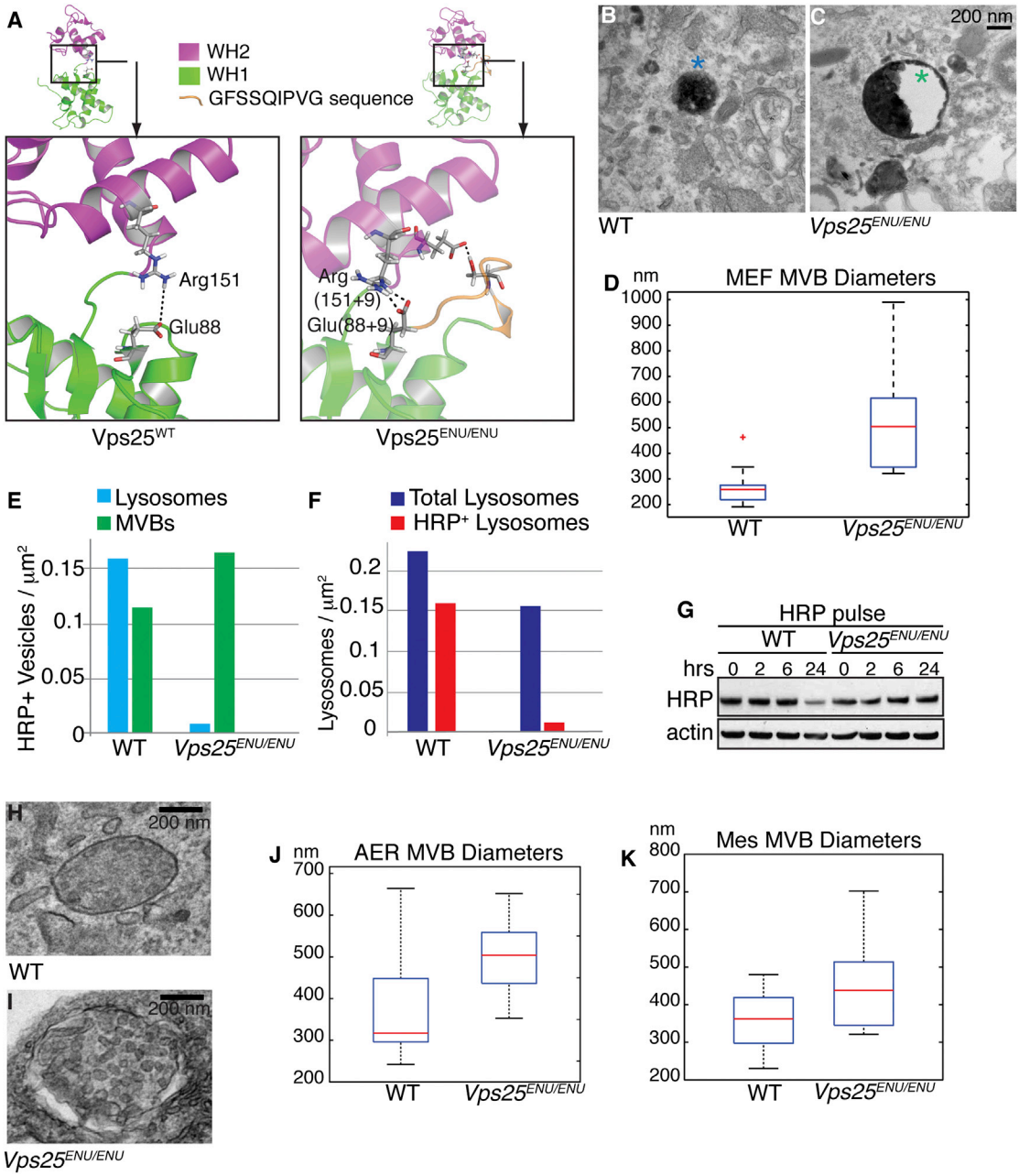

Figure 5. *Vps25* ENU-Induced Mutation Yields Low Levels of Both WT and Structurally Altered Mutant Protein and Is Associated with Engorged MVBs in Cultured Cells, Limb AER, and Mesenchyme In Vivo, Resulting in Perturbed Endosomal Trafficking

(A) Structural representation of WT and $Vps25^{ENU}$ proteins reveals a conserved Glu88-Arg151 hydrogen bond between WH1 (green) and WH2 (magenta) domains. In the $Vps25^{ENU}$ protein, a new strong hydrogen bond (<2 Å) Ser(IV)-Glu(105+9) is formed, due to the nine amino acid insertion (orange). See also Figure S5.

(B–D) Transmission Electron Microscopy (TEM) reveals a significant increase in the diameters of multivesicular bodies (MVBs) in E13.5 mutant versus WT MEFs treated with HRP. The box and whisker plot (D) depicts MVB diameters (in nanometers, nm) on the y axis and WT and $Vps25^{ENU/ENU}$ MVB sample populations on the x axis. Blue boxes represent the middle 50% of the values of the sample range; red lines represent the value of the median sample; legs and bars represent upper and lower limits of the diameter sample. Red cross indicates an outlier. Diameters measured in 16 WT and 12 mutant MVBs (***$p < 0.0001$).

(E) One hundred MVBs and 100 lysosomes counted in HRP-treated WT and mutant MEFs. In WT MEFs, HRP-positive MVBs (green) and lysosomes (blue) are present in approximately equal numbers, whereas in $Vps25^{ENU/ENU}$ MEFs HRP-positive lysosomes are negligible.

(F) Numbers of total (purple) and HRP-positive (red) lysosomes (100) counted and reported per surface areas (mm^2) in both WT and $Vps25^{ENU/ENU}$ MEFs, showing that in mutant MEFs HRP is not escorted to the lysosomes.

(G) WB analysis of MEFs treated with a 30 min HRP pulse and chased for different times (hours, hrs), demonstrates abnormal HRP degradation in mutant MEFs.

(legend continued on next page)

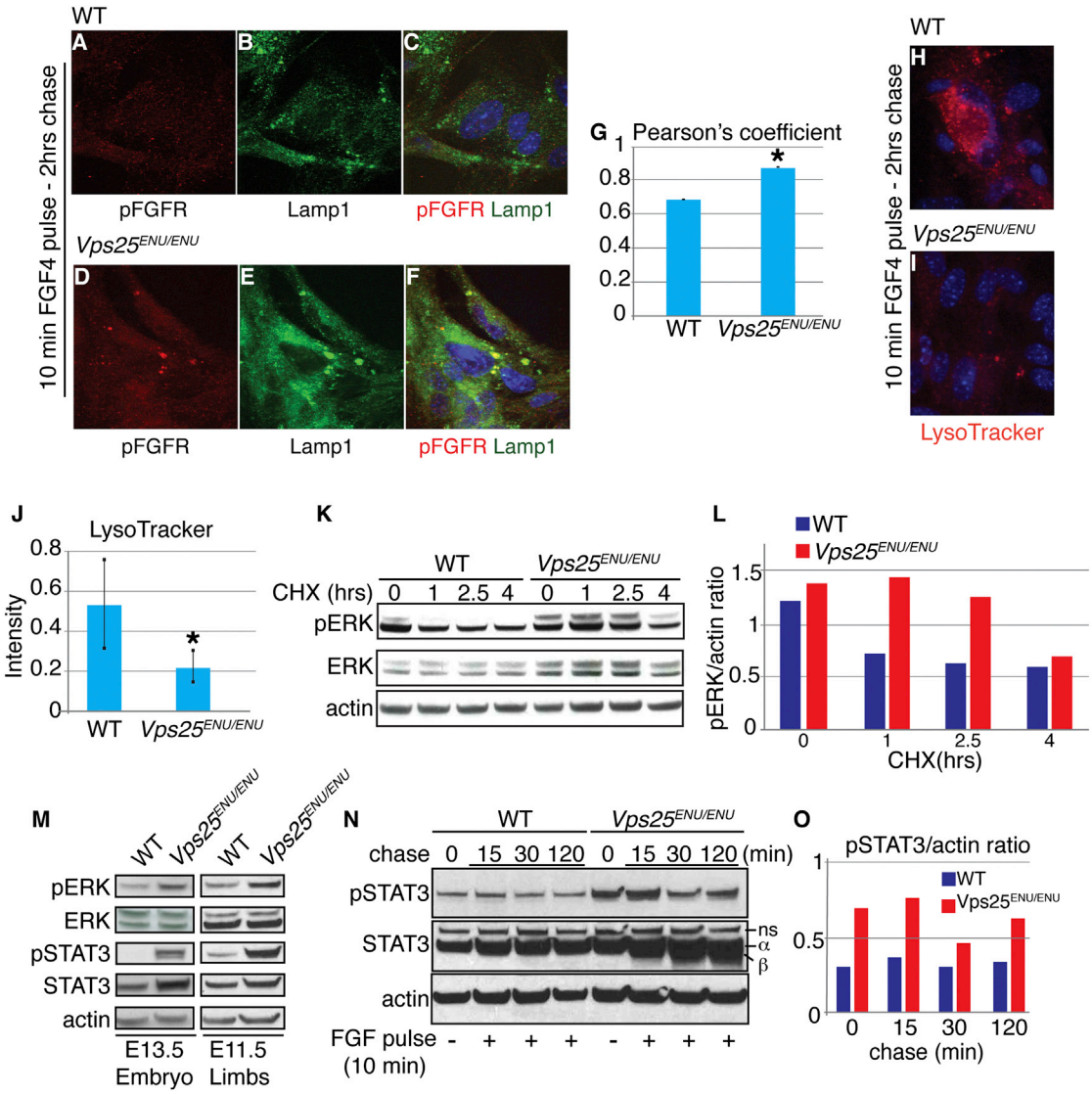

Figure 6. Vps25 ENU-Induced Mutation Results in FGF Receptor Degradation Defects and Enhancement of FGF Signaling in Both Cultured Cells and Limb Buds In Vivo

(A–G) IF for phospho(p)-FGFR following FGF4 pulse-chase in MEFs shows increased colocalization of pFGFR and Lamp1 in late endosomes (or MVBs) of mutant MEFs versus WT, quantified by Pearson's coefficient (*$p < 0.05$), indicating MVB sequestration of pFGFR. Error bars represent the SEM.

(H–J) After a 10 min FGF4 pulse, WT and *Vps25*$^{ENU/ENU}$ MEFs were chased for 2 hr (hrs) and vesicular pH measured by LysoTracker staining. Quantification of signal intensity reveals significantly lower levels of staining in *Vps25*$^{ENU/ENU}$ MEFs, indicating lysosomal functionality defects (*$p < 0.05$). Error bars represent the SEM.

(K and L) Assessment of pERK protein stability in WT and *Vps25*$^{ENU/ENU}$ MEFs treated with cycloheximide (CHX) for different times, indicated in hours, demonstrates abnormal protein degradation in mutant cells. ERK and actin as controls. Quantification of pERK levels over actin by ImageJ64 in WT (purple) and *Vps25*$^{ENU/ENU}$ (red) MEFs (L).

(M–O) WB of whole embryos (E13.5) and limbs (E11.5), as well as FGF4 pulse-chase experiment in MEFs, show increase of FGF second messengers and decreased pSTAT3 degradation, quantified by ImageJ64, in *Vps25*$^{ENU/ENU}$ (red) versus WT (purple) MEFs. Actin as control. min, minutes; ns, nonspecific band.

High-Resolution Mapping and Transcriptome Analysis for Gene Cloning

To clone the gene responsible for the ENU-induced mutation, classic procedures combining whole-genome SNP (Moran et al., 2006) mapping with gene expression microarray analysis for gene finding were used. Total RNA from E12.5 WT and homozygous mutant embryos from line *04-014* was purified using the RNeasy kit (QIAGEN). Roche NimbleGen 12plex HD2 gene expression microarrays (design number 100718_MM9 _exp_HX12) were

(H–K) TEM reveals a significant increase in MVB diameters within the limb AER and mesenchyme compartments of E11.5 *Vps25*$^{ENU/ENU}$ (n = 5) versus WT (n = 2) embryos. The box-and-whisker plots (J and K), as detailed above (in D), depict MVB diameters (in nanometers, nm) on the y axis and WT and *Vps25*$^{ENU/ENU}$ MVB sample populations on the x axis. Diameters measured in 13 WT and 12 mutant MVBs, in limb AER (*$p < 0.05$). In limb mesenchyme, diameters measured in 15 WT and 21 mutant MVBs (*$p < 0.05$).

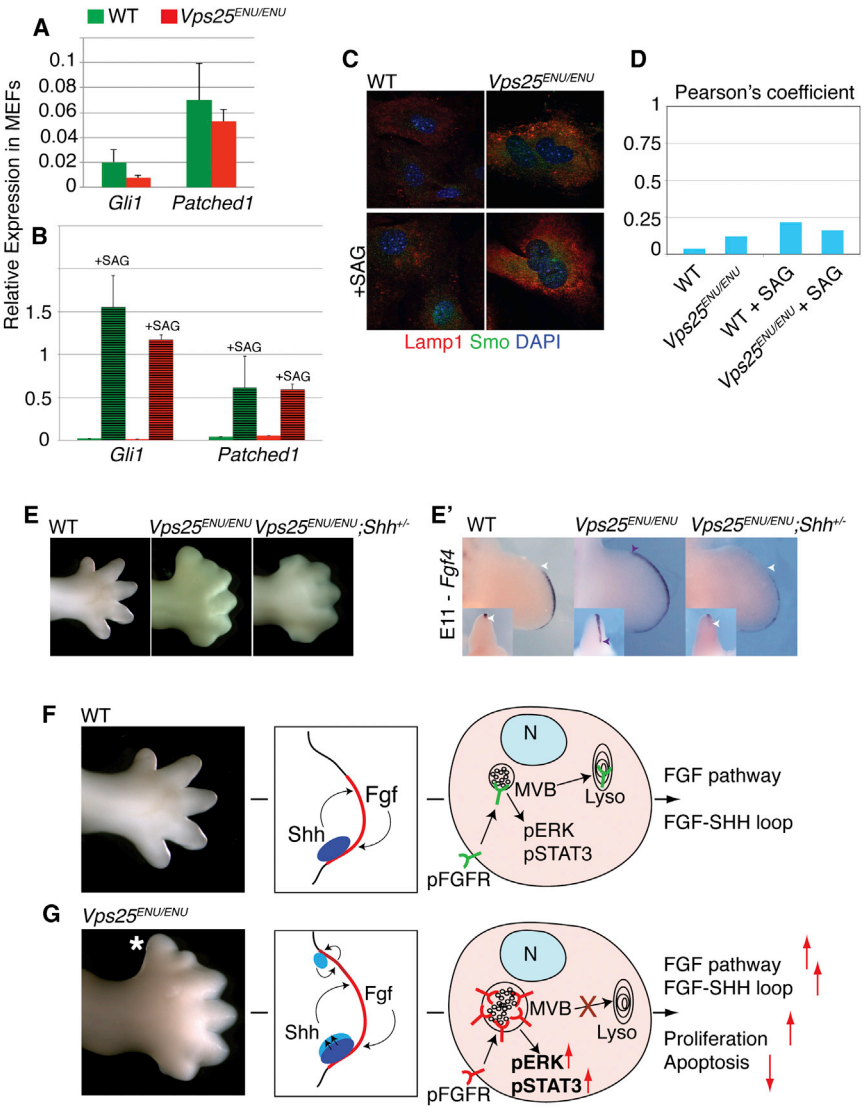

Figure 7. Vps25 ENU-Induced Mutation Does Not Cause Intrinsic Enhancement of SHH Signaling in Cultured Cells, whereas in *Vps25*$^{ENU/ENU}$ Embryo Polydactyly Is Partially Rescued by Limiting the FGF-SHH Feedback Loop

(A and B) qRT-PCR of *Gli1* and *Patched1* in WT (green) and *Vps25*$^{ENU/ENU}$ (red) MEFs, with (dashed bar) and without (solid bar) SAG treatment, demonstrates lack of statistically significant changes of both transcripts in WT versus mutant MEFs. (A) Independent MEF populations derived from three WT and three *Vps25*$^{ENU/ENU}$ embryos analyzed for biological replicates. (B) Independent MEF populations derived from one WT and 1 *Vps25*$^{ENU/ENU}$ embryo analyzed in technical triplicates. In (A) and (B), error bars represent the SEM. (C and D) IF for Smoothened (Smo) (green) and Lamp1 (red) shows no accumulation of Smo in the engorged late endosomes of mutant MEFs, untreated or stimulated with SAG. Pearson's coefficient analysis of Smo trafficking confirms lack of colocalization of Smo and engorged Lamp1-positive endosomes in *Vps25*$^{ENU/ENU}$ MEFs untreated or stimulated with SAG (D). Engorged Lamp1-positive endosomes identified based on a mask selecting for pixels that are among the top 55% in Lamp1 signal intensity.

(E and E′) Partial rescue of digit number and reduction of anterior AER *Fgf4* expansion in *Vps25*$^{ENU/ENU}$;*Shh*$^{+/-}$ mutant HL buds. Normal *Fgf4* expression domain; white arrowheads. *Fgf4* spatial expansion; purple arrowheads.

(F and G) ESCRT-II/Vps25 constrains digit number during development by endosome-mediated selective modulation of the FGF-SHH signaling loop. Substantial loss of Vps25 WT and concomitant presence of Vps25 mutant protein, resulting from the ENU-induced mutation, lead to abnormal accumulation of pFGFR within engorged MVBs and perturbed trafficking to the lysosomes, producing increased levels of FGF second messengers. This triggers hyperactivation of FGF signaling that enhances the FGF-SHH feedback loop, yielding increased proliferation and decreased apoptosis in the limb bud. Overall, this causes polydactyly.

See also Figure S7.

used to analyze expression of all genes within the narrowest critical interval (500 kb) linked to the ENU-induced mutation. cDNA from total RNA was amplified/labeled using Cy3-coupled random nonamers. Technical triplicate hybridizations were performed per sample. Hybridizations were conducted using 4 μg of labeled cDNA per subarray, as per the Roche NimbleGen Gene Expression Protocol. The array data were analyzed using ArrayStar software v.4.0.2 (DNASTAR). Both the mutant and control technical replicates were normalized together, and p values were generated for all expression changes. Pairwise comparisons of global gene expression calls between any two of the technical triplicates per sample correlated with R-squared values of greater than 0.97.

Custom Sureselect Capture and SOLiD Sequencing

DNA capture was performed on 3 μg of high-quality genomic DNA using a custom SureSelect Target Enrichment kit (protocol by Agilent). Chromosome 11 enriched DNA libraries were sequenced on a SOLiD 3plus system (Life Technologies). Twenty-two million reads were generated; 79.7% of the reads were on target, and 95.3% of the target was covered at 10×.

Phenotypic Analysis of *04-014* Embryos

Skeletal preparations, in situ hybridizations, X-Gal stainings, and OPT imaging were carried out as described previously (Ferretti et al., 2011; Sharpe et al., 2002).

Proliferation and Apoptosis Assays

Protocols were as described previously (Ferretti et al., 2011).

mRNA Isolation, RT- PCR, and qRT-PCR

Total RNA was purified from embryos, embryonic limbs, or mouse embryonic fibroblasts (MEFs) at E10.5–13.5 using standard procedures. Gene expression was determined by quantitative real-time PCR using QuantiTect SYBR Green PCR master mix (QIAGEN) or predesigned TaqMan Gene expression Assays and the 7500 Real-Time PCR System (Applied Biosystems).

Generation of *Vps25* Global LOF Allele

Vps25 global LOF was obtained by insertion of a *LacZ* cassette into the gene locus (*Vps25*$^{tm1(KOMP)Vlcg/+}$) (trans-NIH Knock-Out Mouse Project [KOMP]). All

animal experiments were performed following protocols approved by the WCMC IACUC.

Immunohistofluorescence and Whole-Mount LysoTracker

Embryos were cryosectioned for immunofluorescence (IF) experiments or incubated with LysoTracker (Naiche and Papaioannou, 2007) to detect whole-mount staining.

Cell Culture

MEFs were isolated according to standard protocols from E11.5–13.5 WT and *Vps25*$^{ENU/ENU}$ embryos. MEFs were pulse-chased with FGF4 for various time points as indicated or treated for 24 hr with SAG (Goetz et al., 2009) and tested for different markers by IF and qRT-PCR. Cell trafficking was investigated by LysoTracker staining and horseradish peroxidase (HRP) uptake experiments (Shim et al., 2006). For HRP uptake experiments, cells were incubated with 100 μg/ml HRP for 1 hr and then chased for different times as indicated. For HRP uptake experiments followed by transmission electron microscopy (TEM), cells were serum starved prior to stimulation with 5 mg/ml HRP for 30 min and then fixed and crosslinked with 3,3′-diaminobenzidine (DAB) and prepared for TEM. The protein synthesis inhibitor cycloheximide (CHX) was used to treat MEFs (50 μg /ml) as indicated, in order to examine pERK protein degradation, after which cells were lysed for western blotting (WB).

In Vitro Transient Transfection Assays

HEK293 were cultured in DMEM supplemented with 10% fetal calf serum, 2 mM L-glutamine (Invitrogen), in humidified 5% CO_2. Transient transfections were performed using LT1 reagent (Mirus) at a 5:2 ratio. Cells were fixed for immunostaining or harvested in NP40 buffer for coimmunoprecipitation (IP) 36 hr after transfection.

Immunoprecipitations and Western Blot Analysis

HEK293 cells were transfected with HA- or FLAG-tagged constructs to conduct IP and WB using HA (mouse, Covance; goat, Santa Cruz Biotechnology) or FLAG (Sigma-Aldrich) Ab. For IP and coIP, cells were lysed in NP40 and incubated overnight with appropriate primary Ab, magnetic beads were applied for 2 hr, and then complexes were dissociated using DTT before WB analysis. WB was performed using whole embryos, limbs, MEFs, or HEK293 cells. Samples were lysed in RIPA buffer, and proteins were separated on a 4%–12% precast gel followed by transfer to 0.2% nitrocellulose membranes. Primary Abs were incubated in blocking solution overnight at 4°C and blotted with the relevant secondary Abs.

Computational Approach to 3D Modeling of Vps25^{WT} and Vps25^{ENU} Mutant Proteins

For computational modeling and simulation studies designed to distinguish differences in structure and dynamics between Vps25^{WT} and Vps25^{ENU}, the molecular models of the two constructs were immersed in a restrained water sphere (Phillips et al., 2005) for extensive dynamics simulations. Six separate simulations were done, consisting of triplicate repeats for Vps25^{WT} and Vps25^{ENU}.

Transmission Electron Microscopy

MEFs and isolated limb buds were processed following standard procedures (Venable and Coggeshall, 1965). Two WT and five *Vps25*$^{ENU/ENU}$ mutant embryos at E11.5 were imaged to visualize MVBs in limb AER and mesenchyme compartments. MVB diameters measured using ImageJ64 and MATLAB (MathWorks).

Statistical Analysis

Results are given as the average ±SD or SEM. Statistical analyses were performed with Excel (Microsoft) applying the two-tailed t test. p values < 0.05 were considered significant.

Calculation of Pearson's Coefficient

MATLAB (MathWorks) was used to calculate colocalization of IF signals.

SUPPLEMENTAL INFORMATION

Supplemental Information includes Supplemental Experimental Procedures, six figures, and four movies and can be found with this article online at http://dx.doi.org/10.1016/j.celrep.2014.09.019.

AUTHOR CONTRIBUTIONS

K.H. and J.F. conducted high-resolution mapping; identified *Vps25* mutation; completed genetic complementation; performed skeletal preparations, ISH, IF, TEM, IP, WB, and genetic rescue experiments; and assisted L.S. in manuscript writing. M.K. participated in the ENU screen, conducted high-resolution mapping, cloned tagged Vps20 and Vps25 WT and mutant expression constructs, and performed qRT-PCR for *Vps25* expression levels. E.F. participated in the ENU screen, performed skeletal preparations, and conducted initial high-resolution mapping. M.R. performed qRT-PCR for *Shh*, *Patched1*,and *Gli1* in limb buds and MEFs; performed statistical analyses; and contributed to manuscript writing. R.Z. established that the Vps25 mutation is hypomorphic by WB, generated MEF lines, and contributed to manuscript writing. M.A.S. and H.W. conducted 3D modeling of WT and Vps25^{ENU} proteins and contributed to manuscript writing. J.-D.B. provided qRT-PCR primers for *Shh*, *Patched1*, and *Gli1* and assisted the interpretation of limb ISH data. X.P.P. identified involvement of pSTAT3 as second messenger of FGF hyperactivation. M.D. analyzed skeletal preparations of all ENU-mutagenized lines. L.Q. and J.S. performed OPT and 3D analysis of limbs for Vps25 mutant line. B.W. provided a Gli3 antibody. H.A. assisted in deep sequencing. R.R. conducted embryo dissections throughout ENU screen. S.B. and J.R.M. conducted microarray experiments and analyses for gene finding. T.V. performed analyses of MVB and lysosomal diameters and provided suggestions to explore abnormal ESCRT function. K.V.A. initiated the ENU screen and gave input for high-resolution mapping and analysis of the SHH pathway. E.L. participated in the ENU screen and in analysis and interpretation of all data. L.S. conducted embryo dissections throughout ENU screen; designed the project; and wrote the manuscript.

ACKNOWLEDGMENTS

This study was funded by grants R21DE018031, R21DE018031-02S1, and 2R01HD043997 to L.S. ESC clones with Vps25 LOF were obtained from KOMP. NIH grants to Velocigene at Regeneron, Inc. (U01HG004085) and the CSD Consortium (U01HG004080) funded the generation of gene-targeted ESCs for 8,500 genes (KOMP Program) distributed by UC Davis and CHORI (U42RR024244). We thank David Beier, Jennifer Moran, and Tim McGraw for stimulating discussions; Wesley I. Sundquist for invaluable suggestions and the generous gift of a VPS25 polyclonal antibody; Leona Cohen-Gould for TEM; Agnes Viale and Nicholas D. Socci for deep sequencing; and Mu He for technical suggestions. We thank Robert Aho for data analyses and artwork composition.

Received: December 30, 2013
Revised: August 6, 2014
Accepted: September 9, 2014
Published: October 16, 2014

REFERENCES

Anderson, K.V., and Ingham, P.W. (2003). The transformation of the model organism: a decade of developmental genetics. Nat. Genet. Suppl. *33*, 285–293.

Anderson, E., Peluso, S., Lettice, L.A., and Hill, R.E. (2012). Human limb abnormalities caused by disruption of hedgehog signaling. Trends Genet. *28*, 364–373.

Arnold, C.N., Xia, Y., Lin, P., Ross, C., Schwander, M., Smart, N.G., Müller, U., and Beutler, B. (2011). Rapid identification of a disease allele in mouse through whole genome sequencing and bulk segregation analysis. Genetics *187*, 633–641.

Babst, M., Katzmann, D.J., Estepa-Sabal, E.J., Meerloo, T., and Emr, S.D. (2002a). Escrt-III: an endosome-associated heterooligomeric protein complex required for mvb sorting. Dev. Cell *3*, 271–282.

Babst, M., Katzmann, D.J., Snyder, W.B., Wendland, B., and Emr, S.D. (2002b). Endosome-associated complex, ESCRT-II, recruits transport machinery for protein sorting at the multivesicular body. Dev. Cell *3*, 283–289.

Biesecker, L.G. (2011). Polydactyly: how many disorders and how many genes? 2010 update. Dev. Dyn. *240*, 931–942.

Bouldin, C.M., and Harfe, B.D. (2009). Aberrant FGF signaling, independent of ectopic hedgehog signaling, initiates preaxial polydactyly in Dorking chickens. Dev. Biol. *334*, 133–141.

Chanut-Delalande, H., Jung, A.C., Baer, M.M., Lin, L., Payre, F., and Affolter, M. (2010). The Hrs/Stam complex acts as a positive and negative regulator of RTK signaling during Drosophila development. PLoS ONE *5*, e10245.

Chen, P., Zhang, L., Weng, T., Zhang, S., Sun, S., Chang, M., Li, Y., Zhang, B., and Zhang, L. (2014). A Ser252Trp mutation in fibroblast growth factor receptor 2 (FGFR2) mimicking human Apert syndrome reveals an essential role for FGF signaling in the regulation of endochondral bone formation. PLoS ONE *9*, e87311.

Chiang, C., Litingtung, Y., Harris, M.P., Simandl, B.K., Li, Y., Beachy, P.A., and Fallon, J.F. (2001). Manifestation of the limb prepattern: limb development in the absence of sonic hedgehog function. Dev. Biol. *236*, 421–435.

Ferretti, E., Li, B., Zewdu, R., Wells, V., Hebert, J.M., Karner, C., Anderson, M.J., Williams, T., Dixon, J., Dixon, M.J., et al. (2011). A conserved Pbx-Wnt-p63-Irf6 regulatory module controls face morphogenesis by promoting epithelial apoptosis. Dev. Cell *21*, 627–641.

Gibbings, D.J., Ciaudo, C., Erhardt, M., and Voinnet, O. (2009). Multivesicular bodies associate with components of miRNA effector complexes and modulate miRNA activity. Nat. Cell Biol. *11*, 1143–1149.

Goetz, R., and Mohammadi, M. (2013). Exploring mechanisms of FGF signalling through the lens of structural biology. Nat. Rev. Mol. Cell Biol. *14*, 166–180.

Goetz, S.C., Ocbina, P.J., and Anderson, K.V. (2009). The primary cilium as a Hedgehog signal transduction machine. Methods Cell Biol. *94*, 199–222.

Hart, K.C., Robertson, S.C., Kanemitsu, M.Y., Meyer, A.N., Tynan, J.A., and Donoghue, D.J. (2000). Transformation and Stat activation by derivatives of FGFR1, FGFR3, and FGFR4. Oncogene *19*, 3309–3320.

Henne, W.M., Buchkovich, N.J., and Emr, S.D. (2011). The ESCRT pathway. Dev. Cell *21*, 77–91.

Henne, W.M., Stenmark, H., and Emr, S.D. (2013). Molecular mechanisms of the membrane sculpting ESCRT pathway. Cold Spring Harb. Perspect. Biol. *5*, 9.

Im, Y.J., and Hurley, J.H. (2008). Integrated structural model and membrane targeting mechanism of the human ESCRT-II complex. Dev. Cell *14*, 902–913.

Im, Y.J., Wollert, T., Boura, E., and Hurley, J.H. (2009). Structure and function of the ESCRT-II-III interface in multivesicular body biogenesis. Dev. Cell *17*, 234–243.

Irion, U., and St Johnston, D. (2007). bicoid RNA localization requires specific binding of an endosomal sorting complex. Nature *445*, 554–558.

Itoh, N., and Ornitz, D.M. (2004). Evolution of the *Fgf* and *Fgfr* gene families. Trends Genet. *20*, 563–569.

Jimenez, A.J., Maiuri, P., Lafaurie-Janvore, J., Divoux, S., Piel, M., and Perez, F. (2014). ESCRT machinery is required for plasma membrane repair. Science *343*, 1247136.

Komada, M., and Soriano, P. (1999). Hrs, a FYVE finger protein localized to early endosomes, is implicated in vesicular traffic and required for ventral folding morphogenesis. Genes Dev. *13*, 1475–1485.

Koss, M., Bolze, A., Brendolan, A., Saggese, M., Capellini, T.D., Bojilova, E., Boisson, B., Prall, O.W., Elliott, D.A., Solloway, M., et al. (2012). Congenital asplenia in mice and humans with mutations in a Pbx/Nkx2-5/p15 module. Dev. Cell *22*, 913–926.

Lallemand, Y., Bensoussan, V., Cloment, C.S., and Robert, B. (2009). Msx genes are important apoptosis effectors downstream of the Shh/Gli3 pathway in the limb. Dev. Biol. *331*, 189–198.

Langelier, C., von Schwedler, U.K., Fisher, R.D., De Domenico, I., White, P.L., Hill, C.P., Kaplan, J., Ward, D., and Sundquist, W.I. (2006). Human ESCRT-II complex and its role in human immunodeficiency virus type 1 release. J. Virol. *80*, 9465–9480.

Lee, J.A., Beigneux, A., Ahmad, S.T., Young, S.G., and Gao, F.B. (2007). ESCRT-III dysfunction causes autophagosome accumulation and neurodegeneration. Curr. Biol. *17*, 1561–1567.

Lopez-Rios, J., Speziale, D., Robay, D., Scotti, M., Osterwalder, M., Nusspaumer, G., Galli, A., Holländer, G.A., Kmita, M., and Zeller, R. (2012). GLI3 constrains digit number by controlling both progenitor proliferation and BMP-dependent exit to chondrogenesis. Dev. Cell *22*, 837–848.

Lu, P., Minowada, G., and Martin, G.R. (2006). Increasing Fgf4 expression in the mouse limb bud causes polysyndactyly and rescues the skeletal defects that result from loss of Fgf8 function. Development *133*, 33–42.

MacGurn, J.A., Hsu, P.C., and Emr, S.D. (2012). Ubiquitin and membrane protein turnover: from cradle to grave. Annu. Rev. Biochem. *81*, 231–259.

Mariani, F.V., and Martin, G.R. (2003). Deciphering skeletal patterning: clues from the limb. Nature *423*, 319–325.

Moran, J.L., Bolton, A.D., Tran, P.V., Brown, A., Dwyer, N.D., Manning, D.K., Bjork, B.C., Li, C., Montgomery, K., Siepka, S.M., et al. (2006). Utilization of a whole genome SNP panel for efficient genetic mapping in the mouse. Genome Res. *16*, 436–440.

Naiche, L.A., and Papaioannou, V.E. (2007). Cre activity causes widespread apoptosis and lethal anemia during embryonic development. Genesis *45*, 768–775.

Naski, M.C., Colvin, J.S., Coffin, J.D., and Ornitz, D.M. (1998). Repression of hedgehog signaling and BMP4 expression in growth plate cartilage by fibroblast growth factor receptor 3. Development *125*, 4977–4988.

Niswander, L., and Martin, G.R. (1993). FGF-4 and BMP-2 have opposite effects on limb growth. Nature *361*, 68–71.

Omi, M., Fisher, M., Maihle, N.J., and Dealy, C.N. (2005). Studies on epidermal growth factor receptor signaling in vertebrate limb patterning. Dev. Dyn. *233*, 288–300.

Ornitz, D.M., and Marie, P.J. (2002). FGF signaling pathways in endochondral and intramembranous bone development and human genetic disease. Genes Dev. *16*, 1446–1465.

Phillips, J.C., Braun, R., Wang, W., Gumbart, J., Tajkhorshid, E., Villa, E., Chipot, C., Skeel, R.D., Kalé, L., and Schulten, K. (2005). Scalable molecular dynamics with NAMD. J. Comput. Chem. *26*, 1781–1802.

Ruland, J., Sirard, C., Elia, A., MacPherson, D., Wakeham, A., Li, L., de la Pompa, J.L., Cohen, S.N., and Mak, T.W. (2001). p53 accumulation, defective cell proliferation, and early embryonic lethality in mice lacking tsg101. Proc. Natl. Acad. Sci. USA *98*, 1859–1864.

Rusten, T.E., Vaccari, T., and Stenmark, H. (2012). Shaping development with ESCRTs. Nat. Cell Biol. *14*, 38–45.

Selever, J., Liu, W., Lu, M.F., Behringer, R.R., and Martin, J.F. (2004). Bmp4 in limb bud mesoderm regulates digit pattern by controlling AER development. Dev. Biol. *276*, 268–279.

Sharpe, J., Ahlgren, U., Perry, P., Hill, B., Ross, A., Hecksher-Sørensen, J., Baldock, R., and Davidson, D. (2002). Optical projection tomography as a tool for 3D microscopy and gene expression studies. Science *296*, 541–545.

Sheth, R., Marcon, L., Bastida, M.F., Junco, M., Quintana, L., Dahn, R., Kmita, M., Sharpe, J., and Ros, M.A. (2012). Hox genes regulate digit patterning by controlling the wavelength of a Turing-type mechanism. Science *338*, 1476–1480.

Shim, J.H., Xiao, C., Hayden, M.S., Lee, K.Y., Trombetta, E.S., Pypaert, M., Nara, A., Yoshimori, T., Wilm, B., Erdjument-Bromage, H., et al. (2006). CHMP5 is essential for late endosome function and down-regulation of receptor signaling during mouse embryogenesis. J. Cell Biol. *172*, 1045–1056.

Slater, R., and Bishop, N.E. (2006). Genetic structure and evolution of the Vps25 family, a yeast ESCRT-II component. BMC Evol. Biol. *6*, 59.

Stottmann, R.W., and Beier, D.R. (2010). Using ENU mutagenesis for phenotype-driven analysis of the mouse. Methods Enzymol. *477*, 329–348.

Sun, X., Mariani, F.V., and Martin, G.R. (2002). Functions of FGF signalling from the apical ectodermal ridge in limb development. Nature *418*, 501–508.

Tabin, C., and Wolpert, L. (2007). Rethinking the proximodistal axis of the vertebrate limb in the molecular era. Genes Dev. *21*, 1433–1442.

Taelman, V.F., Dobrowolski, R., Plouhinec, J.L., Fuentealba, L.C., Vorwald, P.P., Gumper, I., Sabatini, D.D., and De Robertis, E.M. (2010). Wnt signaling requires sequestration of glycogen synthase kinase 3 inside multivesicular endosomes. Cell *143*, 1136–1148.

Teis, D., Saksena, S., and Emr, S.D. (2008). Ordered assembly of the ESCRT-III complex on endosomes is required to sequester cargo during MVB formation. Dev. Cell *15*, 578–589.

Teis, D., Saksena, S., Judson, B.L., and Emr, S.D. (2010). ESCRT-II coordinates the assembly of ESCRT-III filaments for cargo sorting and multivesicular body vesicle formation. EMBO J. *29*, 871–883.

Thompson, B.J., Mathieu, J., Sung, H.H., Loeser, E., Rørth, P., and Cohen, S.M. (2005). Tumor suppressor properties of the ESCRT-II complex component Vps25 in Drosophila. Dev. Cell *9*, 711–720.

Tognon, E., Wollscheid, N., Cortese, K., Tacchetti, C., and Vaccari, T. (2014). ESCRT-0 is not required for ectopic Notch activation and tumor suppression in Drosophila. PLoS ONE *9*, e93987.

Vaccari, T., and Bilder, D. (2005). The *Drosophila* tumor suppressor *vps25* prevents nonautonomous overproliferation by regulating notch trafficking. Dev. Cell *9*, 687–698.

Venable, J.H., and Coggeshall, R. (1965). A simplified lead citrate stain for use in electron microscopy. J. Cell Biol. *25*, 407–408.

Verheyden, J.M., and Sun, X. (2008). An Fgf/Gremlin inhibitory feedback loop triggers termination of limb bud outgrowth. Nature *454*, 638–641.

Wang, B., Fallon, J.F., and Beachy, P.A. (2000). Hedgehog-regulated processing of Gli3 produces an anterior/posterior repressor gradient in the developing vertebrate limb. Cell *100*, 423–434.

Wolpert, L. (1994). Do we understand development? Science *266*, 571–572.

Yamada, M., Ishii, N., Asao, H., Murata, K., Kanazawa, C., Sasaki, H., and Sugamura, K. (2002). Signal-transducing adaptor molecules STAM1 and STAM2 are required for T-cell development and survival. Mol. Cell. Biol. *22*, 8648–8658.

Zakany, J., and Duboule, D. (2007). The role of Hox genes during vertebrate limb development. Curr. Opin. Genet. Dev. *17*, 359–366.

Zeller, R. (2010). The temporal dynamics of vertebrate limb development, teratogenesis and evolution. Curr. Opin. Genet. Dev. *20*, 384–390.

Zeller, R., López-Ríos, J., and Zuniga, A. (2009). Vertebrate limb bud development: moving towards integrative analysis of organogenesis. Nat. Rev. Genet. *10*, 845–858.